# 3D spectral imaging with synchrotron Fourier transform infrared spectro-microtomography

Michael C Martin[1], Charlotte Dabat-Blondeau[1,9], Miriam Unger[2,9], Julia Sedlmair[3,4], Dilworth Y Parkinson[1], Hans A Bechtel[1], Barbara Illman[3,4], Jonathan M Castro[5], Marco Keiluweit[6], David Buschke[7], Brenda Ogle[7], Michael J Nasse[8] & Carol J Hirschmugl[2]

**We report Fourier transform infrared spectro-microtomography, a nondestructive three-dimensional imaging approach that reveals the distribution of distinctive chemical compositions throughout an intact biological or materials sample. The method combines mid-infrared absorption contrast with computed tomographic data acquisition and reconstruction to enhance chemical and morphological localization by determining a complete infrared spectrum for every voxel (millions of spectra determined per sample).**



Synchrotron-based infrared (IR) beamlines provide high–spatial resolution spectroscopy enabling a variety of studies in living cells[1], in biological tissues[2,3] and even of oil-degrading microbes from the recent oil spill in the Gulf of Mexico[4]. Two-dimensional (2D) IR spectromicroscopy has recently become substantially faster via the use of focal plane array (FPA) detectors, which are available at a specialized synchrotron IR beamline called Infrared Environmental Imaging (IRENI) developed at the Synchrotron Radiation Center (SRC) facility[5]. We now use the rapid 2D spectral image acquisition capability of IRENI to measure a large number of projected transmission images as a sample is rotated. For each wavelength, a full 3D representation of the sample is reconstructed via computed tomography algorithms. We produce 4D reconstructions: three spatial dimensions plus a full mid-IR spectral dimension. This method, Fourier transform infrared (FTIR) spectro-microtomography, provides rich spectral information and chemical fingerprinting, including 3D distributions of these signatures throughout the sample.

3D imaging approaches are necessary to study essential cellular functions—such as architecture, mechanical and biochemical triggers, and cell-cell communications—within living tissues[6]. Typical 3D imaging methods use fluorescence and magnetic resonance, requiring labels or contrast agents. To take spectral imaging into the third dimension, others have used confocal depth profiling[7,8] and serial sample sectioning[9], both of which result in a stack of 2D spectral images. Surface-enhanced spatially offset Raman has also recently been used[10] to penetrate deeper into tissues. FTIR spectro-microtomography offers an alternative involving low-energy IR photons that do not affect living systems[11], and it does not require artificial labels, contrast agents or sectioning. This new method greatly enhances the capabilities of both FTIR spectroscopy and tomography by creating a 'full-color' spectro-microtomogram in which colors are assigned by specific chemical identifications or spectral changes. Each voxel contains a complete spectrum, thus providing a wealth of information for advanced spectral segregation techniques such as clustering, neural networks and principal-component analysis. Colocated chemical fingerprints and morphology in 3D reveal internal composition and structure, as demonstrated here with examples from biology, geology, plant sciences, natural minerals and polymers.

Computed tomography is a well-established approach[12] used to reconstruct cross-sectional slices through an object from the transmitted projection images taken as a function of angle around a single axis of rotation. These slices can be stacked to produce a 3D image of the object, which can then be visualized by one of several methods, including volume rendering or digital slicing through the sample along any arbitrary plane. Multiple-energy X-ray tomography can be performed at synchrotron tomography beamlines that can be tuned to, for example, above and below an X-ray absorption edge[13], or multiple elements can be measured by X-ray fluorescence[14]. But, to our knowledge, wide-ranging spectral tomography, particularly that using the power of the mid-IR fingerprint region, has not been shown before. To make FTIR spectro-microtomography possible, we developed a motorized sample mount capable of precisely rotating a sample on a pin mount while holding it at the focus of an IR microscope. Data collection of 2D spectral transmission images as a function of sample angle was automated, and we modified computed tomography reconstruction algorithms to make them spectrally aware, meaning to allow the reconstruction of integrated absorption intensities of specified spectral regions with and without baseline subtractions, differences between spectral regions and full reconstructions

[1]Advanced Light Source Division, Lawrence Berkeley National Laboratory, Berkeley, California, USA. [2]Physics Department, University of Wisconsin–Milwaukee, Milwaukee, Wisconsin, USA. [3]Forest Products Laboratory, US Department of Agriculture Forest Service, Madison, Wisconsin, USA. [4]Synchrotron Radiation Center, University of Wisconsin–Madison, Stoughton, Wisconsin, USA. [5]Institute of Geosciences, University of Mainz, Mainz, Germany. [6]Physical and Life Sciences Directorate, Lawrence Livermore National Laboratory, Livermore, California, USA. [7]Department of Biomedical Engineering, University of Wisconsin–Madison, Madison, Wisconsin, USA. [8]Laboratory for Applications of Synchrotron Radiation, Karlsruhe Institute of Technology, Karlsruhe, Germany. [9]Present addresses: Ecole Nationale Supérieure d'Ingénieurs de Caen, Caen, France (C.D.-B.); Cetics Healthcare Technologies GmbH, Esslingen am Neckar, Germany (M.U.). Correspondence should be addressed to M.C.M. (MCMartin@lbl.gov) or C.J.H. (cjhirsch@uwm.edu).

RECEIVED 13 FEBRUARY; ACCEPTED 2 JULY; PUBLISHED ONLINE 4 AUGUST 2013; DOI:10.1038/NMETH.2596

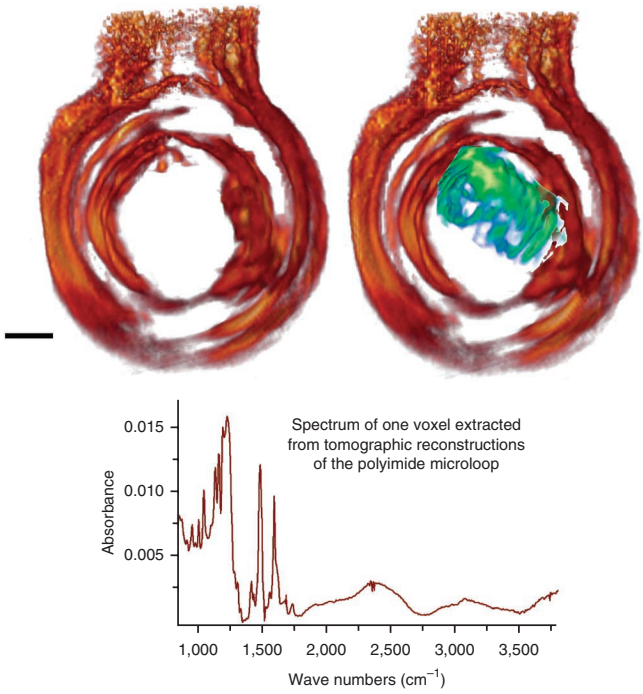


**Figure 1** | FTIR spectro-microtomographic imaging of *Zinnia*. Top, perspective view of a tomographic reconstruction of a *Z. elegans* tracheary element inside a polyimide microloop holder. The red color shows the reconstruction of the integrated intensity from the 2,356.7–2,376.0 $cm^{-1}$ spectral region, where only the sharp edges of the microloop are visualized. The blue-green colors show the reconstruction of the 3,317–3,340 $cm^{-1}$ spectral region associated with OH stretching, highlighting the parallel secondary cell wall thickenings. Reconstructions of this sample were performed at all 816 individual wavelengths measured. Bottom, the intensity of one voxel in the stem of the microloop was reassembled to extract the spectrum of one 1.1 × 1.1 × 1.1 $\mu m^3$ voxel showing a polyimide spectrum with quantitative absorbance matching the volume of the voxel (see Online Methods). Scale bar, 20 µm.

for every wave number measured, which are reassembled into a complete spectrum for every voxel (Online Methods).

Elucidating the 3D molecular architecture of plant cell walls is a challenging problem in plant biology. Although general aspects of cell-wall assembly and synthesis are becoming clear[15], the detailed 3D molecular structure remains poorly understood. A critical step in converting biomass to liquid biofuels and other industrial products is the deconstruction of recalcitrant lignified cell walls; a better understanding of microscale structures and chemical compositions will enhance basic understanding of plant cell walls and will help improve lignocellulose conversion efficiency.

*Zinnia elegans* tracheary elements (individual components of the xylem vascular tissue) comprise a single homogeneous cell type with a known model of *Zinnia* cell-wall architecture[16] and can be cultivated and isolated in the laboratory[17]. We measured and reconstructed a single *Z. elegans* cell inside a MiTeGen polyimide microloop using FTIR spectro-microtomography (**Fig. 1** and **Supplementary Video 1**). Tomographic reconstructions were performed for every wave number such that the reconstructed spectrum of any voxel was extracted by assembling the reconstructed absorbances for that voxel's coordinates. The morphology of the tracheary element and its parallel secondary–cell wall thickenings containing strands of crystalline cellulose microfibrils interspersed with hemicellulose and lignin can be seen when reconstructing the OH-absorption spectral region.

*Populus* is a genus of fast-growing deciduous trees cultivated worldwide for their ecological role in carbon sequestration, nutrient cycling and remediation, and to provide sustainable wood for lumber, fiber for paper, and renewable lignocellulosic biomass for ethanol, nanocellulose and bioplastics. *Populus* species are also models for tree genetics, molecular biology, cell-wall chemistry and biotechnology. A major challenge is to understand the complex, heterogeneous structure of lignocellulose in xylem cell walls.

Reconstructions of a *Populus deltoides* wood sliver (**Fig. 2** and **Supplementary Video 2**) highlight the lignin and holocellulose (hemicellulose and cellulose) distributions and show that the specimen has three longitudinal vessels with the distribution of the hydrocarbon ($CH_2$ and $CH_3$) functional groups filling the

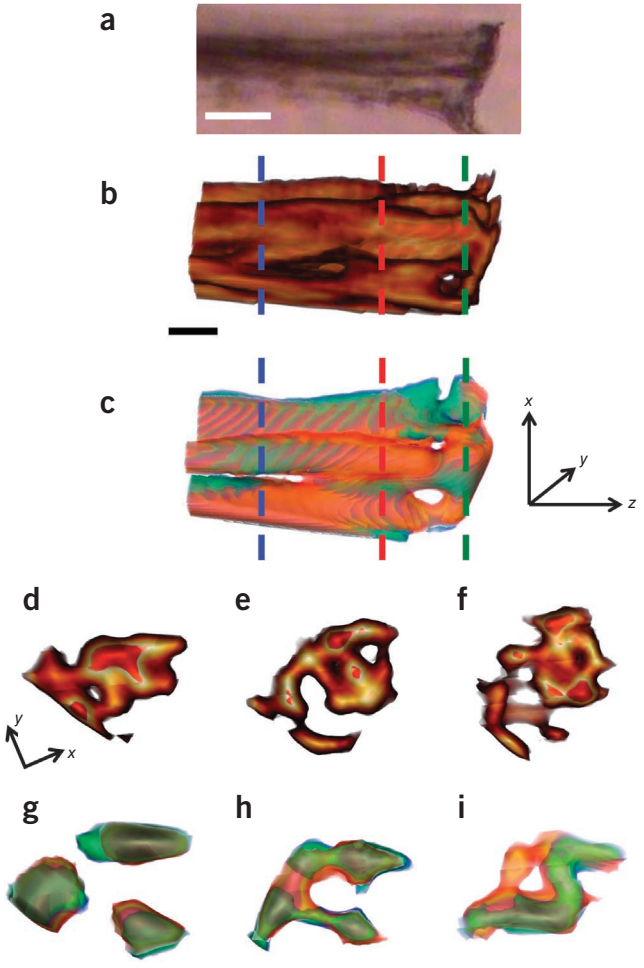


**Figure 2** | Lignocellulose, hemicellulose and CH functional group distributions in a *Populus* wood fiber. (**a**–**c**) Photomicrograph (**a**) and 3D reconstructions (**b**,**c**) of *Populus* wood. (**d**–**i**) Ten-micrometer-thick virtual slices across the vessels at the locations indicated by the dashed lines (blue, **d** and **g**; red, **e** and **h**; green, **f** and **i**). The brown colors in **b** and **d**–**f** are reconstructed intensities of hydrocarbon stretching absorption modes between 2,804–3,023 $cm^{-1}$. The red colors in **c** and **g**–**i** are spectrally associated with lignin (1,523–1,627 $cm^{-1}$) superimposed on the blue-green colors associated with holocellulose (1,689–1,781 $cm^{-1}$). Scale bars, 20 µm.

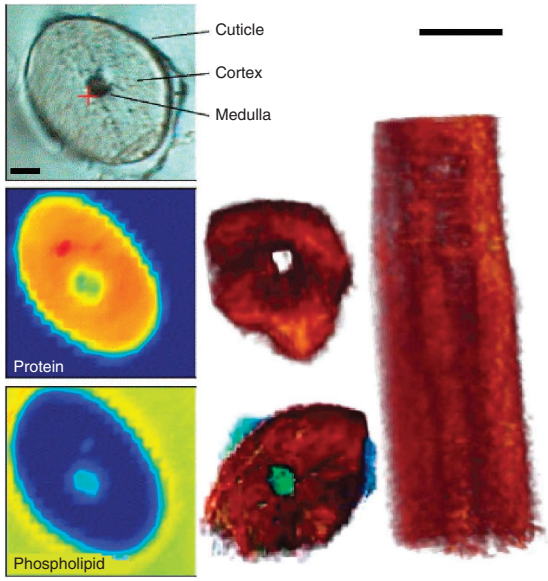


**Figure 3** | 2D and 3D chemical images of hair. Left, visible micrograph (top), with key substructures labeled, and 2D synchrotron IR spectral images of the protein (center) and phospholipid concentrations (bottom) from a cross-section of a human hair (reprinted from ref. 2 with permission from Elsevier). Right, views of the full spectro-microtomographic reconstructions obtained from an intact human hair showing absorptions of protein (red) and phospholipid (blue-green). Center, the medulla is observed to have little protein. Bottom center, the medulla has higher concentrations of phospholipids. Scale bars, 25 μm.

space between the vessels. Virtual slices through the three vessel walls (**Fig. 2g–i**) show that the holocellulose is more prominent in the middle (S2 layer), whereas lignin is more dominant around the exterior of the cells.

Many 3D biomedical samples are sliced with a microtome into thin sections for study. However, the embedding matrix can chemically alter the tissue, and fragile structures of high interest can be destroyed by the embedding and cutting process. In contrast, FTIR spectro-microtomography provides 3D information from intact specimens.

Hair has a distinctive biochemical construction. Reconstructed 3D spectral images from a human hair with no sample preparation reveal the known biochemical morphology (**Fig. 3** and **Supplementary Video 3**). Rotating the reconstruction to look down the axis of the hair, one sees that the protein fills the cortex but not the medulla[2]. The medulla is, however, filled with phospholipids (**Fig. 3**). These spectro-microtomography results demonstrate that spectral reconstructions can be done on larger fully hydrated biological samples and also that we can spectrally identify a fully buried portion of the sample. No time-consuming, potentially damaging and/or sample-modifying embedding and microtome sectioning was needed.

Pluripotent stem cells can assume nearly any functional cell type. Maintaining stem cells outside the body is challenging, however, because cell genotype, phenotype and function can change rapidly and unpredictably. Most approaches for stem cell characterization rely on sample manipulation and are incapable of analyzing intact 3D cell aggregates or tissues—structures known to be crucial for the stem cell state[18].

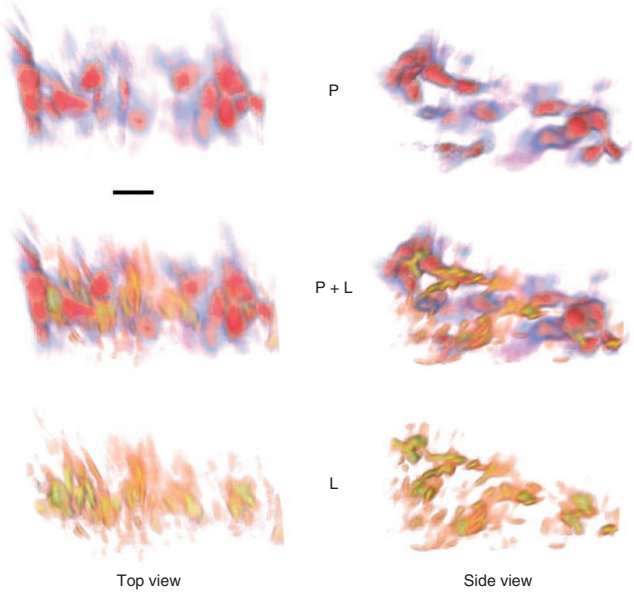


Here an intact mouse embryoid body, comprising 3D aggregates of pluripotent stem cells that can spontaneously differentiate into cells of the three germ layers, was harvested on a polyimide holder 24 h after formation. At this stage, the embryoid body contains primarily pluripotent stem cells and a smaller fraction of differentiating cells. The cell bodies are easily identified from the IR absorptions of peptide bonds in the proteins and isopeptide bonds of protein side chains (**Fig. 4** and **Supplementary Video 4**) and show a layered structure. The embryoid bodies at 24 h are fragile and likely have not yet established tight cell-cell and cell-matrix interactions, a lack that leads to the cell spacing observed in the tomographic images. The lipid-dominated morphology is not distributed uniformly around them. On the basis of recent literature[19–23], we hypothesize that the heterogeneous lipid distribution might correspond to differentiating versus pluripotent or progenitor cell types. This technique has promise not only for stem cell screening without the use of dyes or probes but also for promoting a better understanding of the biochemical structure of differentiating stem cells in their microenvironment.

Methods to produce tissue samples and 3D cell culture samples for FTIR spectro-microtomography need further development. Samples with a cylindrical geometry are optimal for tomographic studies because images can be obtained at all rotation angles. Fine-needle biopsies might therefore provide ideal medically relevant samples, with the biopsied material pushed out of the needle core, or the needle itself could be made of an IR-transparent material such as chalcogenide[24]. 3D cell cultures could be placed in liquid agarose that is spectrally distinct enough for IR imaging[25], drawn up into a microcapillary and then solidified and extracted from the capillary[6] for tomographic analysis.

**Figure 4** | Top and side views of 3D protein and lipid distributions for an embryoid body colony of stem cells. Volume renderings from reconstructions for the protein (P) amide I absorption band (1,650 $cm^{-1}$; blue-red; top) and lipid (L)-specific bands (2,850 $cm^{-1}$; orange-yellow; bottom) reveal three layers of cell bodies with inhomogeneously distributed lipids. The two spectral region reconstructions are shown independently and superimposed (P + L) to provide context for the images. Scale bar, 10 μm.

FTIR spectro-microtomography provides spectrally rich, label-free, nondestructive 3D visualizations of biological and materials samples (**Supplementary Note**). Efficient data collection and analysis facilities with the promise of quantitative analysis are under development at IRENI and Advanced Light Source (ALS) IR beamline 5.4, which will incorporate advances from protein crystallography, X-ray tomography, medical tomography, FTIR spectroscopy, and computational control and analysis to automate the collection, processing and storage of large spectral tomographic data sets. Continued advances in mid-IR array detector technologies, synchrotron IR beamlines and computational tomography tool sets are expected to improve FTIR spectro-microtomography. We anticipate that our method will facilitate a wide variety of scientific, industrial, materials, energy and medical applications.

## METHODS

Methods and any associated references are available in the online version of the paper.

*Note: Any Supplementary Information and Source Data files are available in the online version of the paper.*

**ACKNOWLEDGMENTS**

Thanks to K. Krueger, M. Fisher and G. Rogers for outstanding machining skills and technical support. We also thank D. Ron for assistance on the spectral extractions. This work is based on research conducted at the IRENI beamline, whose construction and development was supported by the US National Science Foundation by award MRI-0619759. This work was supported by the US National Science Foundation under grant CHE-1112433. The ALS is supported by the Director, Office of Science, Office of Basic Energy Sciences, US Department of Energy under contract no. DE-AC02-05CH11231. The SRC is primarily funded by the University of Wisconsin–Madison, with supplemental support from facility users and the University of Wisconsin–Milwaukee.

**AUTHOR CONTRIBUTIONS**

M.C.M. and C.J.H. conceived of the technique and led the project. C.D.-B. wrote automated data analysis code and carried out some of the experiments. M.J.N. wrote scripts to automate the data collection at IRENI. M.U. and J.S. helped perform all experiments. D.Y.P. provided tomographic reconstruction algorithms and expert advice on setting up the experiments. H.A.B. provided optical mount expertise and assistance with analysis codes. B.I. provided *Populus* samples and helped perform experiments and analysis of these samples. J.M.C. provided the volcanic samples and expertise for their analysis. M.K. provided the *Zinnia* samples and expertise for their analysis. D.B. and B.O. provided embryoid body colony samples and expertise for their analysis. All authors helped with writing this paper.

**COMPETING FINANCIAL INTERESTS**

The authors declare no competing financial interests.



1. Holman, H.-Y.N., Bechtel, H.A., Hao, Z. & Martin, M.C. *Anal. Chem.* **82**, 8757–8765 (2010).
2. Miller, L.M. & Dumas, P. *Biomembranes* **1758**, 846–857 (2006).
3. Kastyak-Ibrahim, M.Z. *et al. Neuroimage* **60**, 376–383 (2012).
4. Hazen, T.C. *et al. Science* **330**, 204–208 (2010).
5. Nasse, M.J. *et al. Nat. Methods* **8**, 413–416 (2011).
6. Pampaloni, F., Reynaud, E.G. & Stelzer, E.H.K. *Nat. Rev. Mol. Cell Biol.* **8**, 839–845 (2007).
7. Guilhaumou, N., Dumas, P., Carr, G.L. & Williams, G.P. *Appl. Spectrosc.* **52**, 1029–1034 (1998).
8. Jamme, F., Lagarde, B., Giuliani, A., Garcia, G. & Mercury, L. *J. Phys. Conf. Ser.* **425**, 142002 (2013).
9. McNaughton, D., Wood, B.R., Cox, T.C., Drenckhahn, J.-D. & Bambery, K.R. in *Infrared and Raman Spectroscopic Imaging* (eds. Salzer, R. & Siesler, H.W.) 203–223 (Wiley, 2009).
10. Stone, N. *et al. Chem. Sci.* **2**, 776–780 (2011).
11. Holman, H.-Y.N., Martin, M.C. & McKinney, W.R. *J. Biol. Phys.* **29**, 275–286 (2003).
12. Herman, G.T *Fundamentals of Computerized Tomography: Image Reconstruction from Projection* 2nd edn. (Springer, 2010).
13. Mizutani, R. *et al.* in *Microscopy: Science, Technology, Applications and Education*. Vol. 1 (eds. Mendez-Vilas, A. & Diaz, J.) 379–386 (Formatex Research Centre, 2010).
14. de Jonge, M.D. *et al. Proc. Natl. Acad. Sci. USA* **107**, 15676–15680 (2010).
15. Illman, B.L. & Dowd, B.A. in *Developments in X-Ray Tomography II* Vol. 3772 (ed. Bonse, U.), 198–204 (SPIE, 1999).
16. Lacayo, C.I. *et al. Plant Physiol.* **154**, 121–133 (2010).
17. Fukuda, H. & Komamine, A. *Plant Physiol.* **65**, 57–60 (1980).
18. Buschke, D.G., Eliceiri, K.W. & Ogle, B.M. in *Stem Cell-Based Tissue Repair* (ed. Goradetsky, R.S.) 55–140 (RSC, 2010).
19. Pijanka, J.K. *et al. Analyst* (*Lond.*) **135**, 3126–3132 (2010).
20. Cao, J. *et al. J. Biophotonics* published online, doi:10.1002/jbio.201200217 (25 April 2013).
21. Ye, D. *et al. Analyst* (*Lond.*) **137**, 4774–4784 (2012).
22. Dottori, M., Leung, J., Turnley, A.M. & Pebay, A. *Stem Cells* **26**, 1146–1154 (2008).
23. Sánchez-Sánchez, R. *et al. Dev. Dyn.* **241**, 953–964 (2012).
24. Krishnaswami, K., Qiao, H., Bernacki, B.E. & Anheier, N.C. Jr. in *Laser Technology for Defense and Security V* Vol. 7325 (eds. Dubinskii, M. & Post, S.G.), 73250Z (SPIE, 2009).
25. Nallala, J. *et al. J. Biomed. Opt.* **17**, 116013 (2012).

## ONLINE METHODS

**Synchrotron IR beamline.** Our tomographic experiments were performed at the IRENI beamline at the SRC at the University of Wisconsin–Madison[5,26]. Synchrotron-based IR beamlines provide high–spatial resolution spectromicroscopy at the diffraction limit[27–31]. The IRENI beamline uses 12 beams of synchrotron IR light to illuminate a wide region of a Santa Barbara Focal Plane MCT array (FPA) detector within a Hyperion 3000 IR microscope (Bruker Optics)[5]. The collimated light beams first pass through a Vertex 70 FTIR bench, and OPUS 6.5 software collects and processes FTIR spectra from every pixel in the 128 × 128 detector array. Spectral images from each sample angle were acquired in transmission with a 15× (0.5–numerical aperture (NA)) condenser and a 36× (0.5-NA) objective resulting in an effective projected sample pixel size of 1.1 × 1.1 μm. The condenser is moved slightly out of focus to overlap the 12 synchrotron beams and more smoothly fill the FPA detector. We typically collected IR spectra at 8-$cm^{-1}$ resolution using between 24 and 128 coadditions, acquiring a background spectral image before every tomographic sample measurement.

**Sample holder.** For FTIR spectro-microtomography, we mounted samples on sample holders that are designed for protein crystallography experiments (MiTeGen or Hampton Research). The MiTeGen holders use polyimide that is microfabricated into small loops or other geometries, with 10-μm thickness, mounted to a stainless steel rod. The Hampton Research holders consist of twisted nylon loop with the nylon thread having 10-μm thickness. These two materials have different FTIR spectra and thus have different clear areas for sample spectral features. For example, the polyimide has no CH stretching features around 2,850 and 2,950 $cm^{-1}$ and so these common absorption bands can be observed in many samples without the holder interfering.

**Sample rotation.** For these proof-of-principle experiments, we built an inexpensive sample-rotation and centering stage. The sample holders are mounted on goniometer base type 1A holders (MiTeGen), which are then magnetically mounted onto the head of a 1/4-20 threaded socket head screw with a permanent magnet glued into the socket hole. The screw is placed into an optical post that is mounted in a standard optical post holder allowing for easy manual adjustment for different sample lengths via the set-screw on the post holder. The post is mounted in the center of a tip-tilt optical mount (Thor Labs). The tip-tilt optical mount is then attached to an Agilis piezo-driven rotation stage (Newport Optics). The Agilis rotation stage allows precise rotary motion of the sample driven via a manual or computer controller. To measure the angle of rotation, we mounted a potentiometer with 1 Ω per revolution to the back of the rotary mount, and we clamped it to the nonrotating mounting block. The potentiometer was read out with an ohmmeter having 0.001-Ω sensitivity, meaning the smallest angle change of our sample that we could measure was 0.36°. Finally, all of this was securely mounted to an *x-y-z* positioning stage (Thor Labs) with micrometers for each direction of motion. This tip and tilt of the sample allows positioning of any given part of the sample onto the axis of rotation, and the *x-y-z* positioning allows the positioning of this part of the sample in the center of the FPA field of view. A photograph of this sample mounting setup is shown in **Supplementary Figure 1**. An improved sample-rotation stage is now deployed at IRENI, allowing more accurate automated rotation, and an air-bearing rotation stage with motorized sample tip-tilt adjustments is under development for the ALS.

We used a custom-written macro for OPUS (available upon request) to acquire a series of spectral images. Between each spectral image acquisition we would manually command the rotation stage to move by, for example, 1.8°, as verified by a change of 0.005 Ω on the potentiometer readout. To fully sample the image in Fourier space, images must be collected over at least 180°. The Crowther criterion[32] can be used for an object of certain size ($d$) to determine the resolution ($r$) that can be achieved for a given number of projection images (PI) over 180° ($N$): $r = \mathrm{PI} \times d/N$. We typically used 100 spectral projection images over 180°, with each image having 128 × 128 pixels of spectra.

**Tomographic reconstruction.** Reconstruction for any one wavelength image was accomplished using either filtered back-projection or iterative penalized likelihood tomographic reconstruction from the ASPIRE package[33–37]. A parallel beam was assumed. Although not strictly correct, the beam waist created by the focus at IR wavelengths of the 12 beams (all wavelengths are 3–10 times longer than the effective pixel resolution) is likely approximated reasonably by a parallel beam.

Reconstruction of the transmission image of one wavelength is similar to traditional X-ray tomography. We wrote a series of Java scripts (available upon request) that allow reconstruction of any (or all) of the mid-IR wavelengths to compare absorption features, spectral integrations of wavelength regions corresponding to absorption feature(s), ratios of two absorption band intensities or any of these spectral functions with an automated baseline subtraction. By reconstructing all wavelengths, we can reassemble the reconstructed spectrum for any or every voxel within the 3D space (an example is shown in **Fig. 1**). Having complete spectra for every voxel can help users to interpret chemical and structural variations in different regions of the sample and/or enable more advanced spectral comparisons and allow the use of sorting tools such as principal-component analysis, cluster analysis and other statistical analysis techniques.

Reconstructing a microloop of polyimide for integrations of the 1,573–1,654 $cm^{-1}$ spectral regions show how both absorption and scattering can affect the reconstructions (**Supplementary Fig. 2** and **Supplementary Video 5**). The 1,573–1,654 $cm^{-1}$ region contains characteristic absorption bands of polyimide. The 2,287–2,414 $cm^{-1}$ region does not have any polyimide vibrational modes absorbing the IR light, but diffraction scattering from the sharp edges of the microloop structure are clearly observed in the individual projection images. The resulting reconstructed structure therefore looks 'hollow', as it is dominated by the edges. We observe the correct microloop structure for the 1,573–1,654 $cm^{-1}$ reconstruction, with additional edge enhancement due to diffraction scattering. The thickness of the microloop (nominally 10 μm) is indeed smaller than the thickness of the holder at the top (nominally 25 μm), as given by the manufacturer.

**Spectral reconstructions.** Tomographic reconstructions were performed for every wave number measured (816 wavelengths for 8-$cm^{-1}$ resolution). The reconstructed spectrum of any given voxel is extracted by finding the reconstructed absorbance for

that voxel's coordinates in each wavelength's 3D reconstruction. A comparison between the extracted spectrum of one voxel to the transmission spectrum acquired through the entire sample thickness in the same region of the sample gives comparable spectra (**Supplementary Fig. 3**). This result demonstrates that the detailed absorbance value from the given voxel is preserved throughout the tomographic reconstruction process, and we now have a full spectral reconstruction tool. Note the absorbance intensity of the absorbance bands for an individual voxel (**Supplementary Fig. 3**) is about 35 times weaker than that of a pixel spectrum from a projection image taken from the stem of the polyimide microloop (**Supplementary Fig. 2**). The voxel is only $1.1 \times 1.1 \times 1.1\ \mu m^3$ in volume, whereas the transmission spectrum is from a region approximately 25-μm thick and has a $1.1 \times 1.1\ \mu m^2$ pixel area. Thus, the amount of sample in one voxel is approximately 25 times smaller than that in one projected pixel. This agreement means that specific 3D constructions of voxels can be meaningfully added together to yield a total absorbance spectrum and, therefore, a total amount of a material within a region of interest in a sample.

***Z. elegans* tracheary elements.** To study a single *Zinnia* tracheary element in 3D, one cell was transferred from culture to the goniometer sample mount using a MiTeGen polyimide microloop. Spectral images (100) were acquired through 180° of sample rotation. The sharp edges of the microloop create strong diffraction scattering, so plotting the reconstruction of a wavelength where no fundamental vibrational absorptions are present shows the sharp edges of the microloop sample holder (**Fig. 1**). The smoother *Zinnia* tracheary element in the center of the microloop, however, shows no such scattering. The reconstruction of absorptions due to OH stretching show the tracheary element and its parallel secondary–cell wall thickenings.

***Populus* wood samples.** A manually extracted sliver from a *P. deltoides* tree branch was mounted such that a 50 × 30–μm region was freestanding. We acquired 50 spectral images as the sample rotated through 180°. Tomographic reconstructions were made from spectral integrations of the 1,523–1,627 $cm^{-1}$, 1,689–1,781 $cm^{-1}$ and 2,804–3,023 $cm^{-1}$ regions corresponding respectively to lignin, holocellulose (hemicellulose and cellulose), and $CH_2$ and $CH_3$ vibrational modes.

**Human hair.** A fresh sample of human hair was obtained from one researcher's head. A part of the hair a few millimeters long was mounted freestanding on the goniometer sample stage, and a plastic bag placed around the sample stage was used to shield this flexible sample from ambient air currents as the sample was rotated and data were acquired. Spectral images were acquired of a 140-μm-long region while we rotated the sample along the length of the hair every 1.8° through 180°. Spectral reconstructions were performed to render in 3D the distributions of proteins and phospholipids.

**Mouse embryonic stem cells.** HM1 mouse embryonic stem cells (ESCs) (Open Biosystems) were cultured in Dulbecco's Modified Eagle's Medium (DMEM + GlutaMAX; Invitrogen) with 10% fetal bovine serum (FBS; Invitrogen), 1% penicillin/streptomycin (Lonza), 1% non-essential amino acids (Invitrogen) and 0.0007% (1% of a 35 ml/50 ml solution) β-mercaptoethanol (MP Biomedicals). To maintain pluripotency, medium was supplemented with leukemia inhibitory factor (LIF; Millipore) at 2,000 U/ml and bone morphogenic protein 4 (BMP-4; R&D Systems) at 10 ng/ml (ref. 38). Embryoid bodies (EBs) were made via the hanging drop method (day 0)[39]. ESCs were harvested and resuspended in DMEM + 10% FBS (no LIF or BMP-4) at $4.8 \times 10^3$ cells per ml. This cell suspension was used to make 30-μl hanging drops over 1× PBS in 100-mm Petri dishes. EBs were harvested 24 h after formation (day 1); the average size of the 3D cell clusters was 127 ± 26 μm. EBs were then fixed in 4% paraformaldehyde for 15 min at room temperature on a platform rocker and resuspended in ultrapure water and held in the polyimide microloop holder for analysis on IRENI.

**Volcanic glass sample.** A small volcanic glass filament from the recently erupted Puyehue-Cordón Caulle volcano in Chile was extracted from a volcanic bomb that was rapidly quenched at the time of eruption (**Supplementary Figs. 4** and **5**, **Supplementary Note** and **Supplementary Video 6**). This tiny filament of glass represents a 'frozen-in' record of the formerly high-temperature melt and the magmatic 'water' dissolved within this glass: specifically, molecular ($H_2O$) and hydroxyl groups ($OH^-$) bound to the silicate network are the target of analysis because these species control the physical properties of silicate melts, including its density and viscosity[40,41]. We acquired 50 spectral images over 180° and reconstructed the 3D volume for every spectral point.


26. Hirschmugl, C.J. & Gough, K.M. *Appl. Spectrosc.* **66**, 475–491 (2012).
27. Levenson, E., Lerch, P. & Martin, M.C. *J. Synchrotron Radiat.* **15**, 323–328 (2008).
28. Mattson, E.C., Unger, M., Manandhar, B., Alavi, Z. & Hirschmugl, C.J. *J. Phys. Conf. Ser.* **425**, 142001 (2013).
29. Dumas, P., Jamin, N., Teillaud, J.L., Miller, L.M. & Beccard, B. *Faraday Discuss.* **126**, 289–302 (2004).
30. Martin, M.C. & Dumas, P. in *Spectroscopic Properties of Inorganic and Organometallic Compounds: Techniques, Materials and Applications* Vol. 43 (eds. Yarwood, J., Douthwaite, R. & Duckett, S.B.) 141–165 (Royal Society of Chemistry, 2012).
31. Martin, M.C., Schade, U., Lerch, P. & Dumas, P. *Trends Analyt. Chem.* **29**, 453–463 (2010).
32. Crowther, R., DeRosier, D.J. & Klug, A. *Proc. R. Soc. Lond. A Math. Phys. Sci.* **317**, 319–340 (1970).
33. Fessler, J.A., Ficaro, E.P., Clinthorne, N.H. & Lange, K. *IEEE Trans. Med. Imaging* **16**, 166–175 (1997).
34. Erdogan, H. & Fessler, J.A. *IEEE Trans. Med. Imaging* **18**, 801–814 (1999).
35. Erdogan, H. & Fessler, J.A. *Phys. Med. Biol.* **44**, 2835–2851 (1999).
36. Fessler, J.A. & Rogers, W.L. *IEEE Trans. Image Process.* **5**, 1346–1358 (1996).
37. Stayman, J.W. & Fessler, J.A. *IEEE Trans. Med. Imaging* **19**, 601–615 (2000).
38. Ying, Q.-L., Nichols, J., Chambers, I. & Smith, A. *Cell* **115**, 281–292 (2003).
39. Maltsev, V.A., Rohwedel, J., Hescheler, J. & Wobus, A.M. *Mech. Dev.* **44**, 41–50 (1993).
40. Castro, J.M. & Dingwell, D.B. *Nature* **461**, 780–783 (2009).
41. Castro, J.M., Manga, M. & Martin, M.C. *Geophys. Res. Lett.* **32**, L21307 (2005).






doi:10.1038/nmeth.2596